

## Intergranular Corrosion Characteristics of Super Duplex Stainless Steel at various Interpass Temperatures

Bo-Hee Lee<sup>1,\*</sup>, Haw-Woo Lee<sup>1</sup>, Yong-Taek Shin<sup>2</sup>

<sup>1</sup> Department of Materials Science and Engineering, Dong-A University, Busan, Rep. of Korea.

<sup>2</sup> Department of Naval Architecture and Offshore Engineering, Dong-A University, Busan, Rep. of Korea.

\*E-mail: [bh.lee2500@gmail.com](mailto:bh.lee2500@gmail.com)

Received: 11 June 2015 / Accepted: 15 July 2015 / Published: 28 July 2015

---

The effect of second phase formation on intergranular corrosion at the weldment in super duplex stainless steel was investigated using various interpass temperatures. Using the same alloy compositions and welding process, welding was carried out at interpass temperatures of 50 °C, 150 °C, and 250 °C. As the interpass temperature was increased, the fraction of second phase formation increased, due to increased time spent at the precipitation temperature of the second phase ( $\sigma$ ,  $\chi$ ). Potentiodynamic polarization testing and double loop electrochemical potentiokinetic reactivation (DL-EPR) testing were conducted in order to evaluate the corrosion resistance. In the case of potentiodynamic polarization testing, the  $E_{\text{pit}}$  and  $I_{\text{pit}}$  values varied according to the interpass temperature, and both the  $E_{\text{pit}}$  and  $I_{\text{pit}}$  values decreased as the fraction of the second phase in the weldment increased. Furthermore, the intergranular corrosion resistance was evaluated using DL-EPR testing, and the degree of sensitization increased with increasing interpass temperature. This effect was because the size of surrounding regions containing reduced amounts of Cr increased with increasing second phase fraction.

---

**Keywords:** Super duplex stainless steel, interpass temperature, welding, corrosion resistance,  $\sigma$ -phase formation.

### 1. INTRODUCTION

Super duplex stainless steel is a type of steel in which ferrite and austenite phases are mixed at a 1:1 ratio, combining the outstanding corrosion resistance of austenite steel and the excellent mechanical properties of ferrite steel. Because of these properties, this material is currently receiving much attention for its possible uses in chemical instruments, deep sea structures, the pipelines of offshore plants, and in other offshore structures.[1] In particular, since its pitting resistance equivalent

number (PREN) has a high value of at least 40, the stress resistance to pitting corrosion, crevice cracking, and chlorine is much higher than that of 304 and 316-austenite stainless steel.[2] However, the ratio of austenite and ferrite phases changes according to the precipitation of compounds between metals throughout the welding and heat treatment processes. Changes in the chemical composition and microstructure of super duplex stainless steel after welding are dependent on factors such as the peak temperature, heat input, preheating temperature, and cooling rate. Therefore, when rapid heating/cooling occurs in a process such as welding, the ferrite fraction increases more than the austenite fraction due to a fast cooling rate, and the chromium nitride ( $\text{Cr}_2\text{N}$ ) in the ferrite is precipitated due to the low nitrogen solubility of ferrite.[3]  $\text{Cr}_2\text{N}$  precipitation increases as the ferrite fraction increases, and high ferrite and  $\text{Cr}_2\text{N}$  contents lead to a decrease in low temperature toughness and play the role of nucleation positions for pitting.[4, 5, 6] In order to maintain high corrosion resistance characteristics and mechanical properties through inhibition of  $\text{Cr}_2\text{N}$  precipitation inside the ferrite, the fraction of ferrite phase in the weldment must be kept to a minimum. More than 75 % of the ferrite phase is considered to be inappropriate.[6] Another issue presented by multi-pass welding is that the precipitation of a second phase, such as the  $\sigma$  and  $\chi$ -phases, occurs because a previous pass has been exposed to temperatures in the second phase precipitation range of 600–1000 °C. This is due to the heat cycle of follow-up welding. The  $\sigma$ -phase is formed through a eutectoid reaction,  $\delta$ -ferrite  $\Leftrightarrow \sigma + \gamma_2$ , and as the deficiency regions of Cr and Mo are formed around a hardened structure containing large amount of Cr and Mo, the corrosion resistance is reduced and brittleness is induced.[7, 8] The priority when welding super duplex stainless steel is therefore to inhibit second phase precipitation as much as possible, and to this end, there have been many studies on factors that influence second phase precipitation, such as the welding heat input, alloy composition, and cooling rate. Furthermore, although interpass temperature is related to the cooling rate [9], there have not been sufficient studies on the effect of the interpass temperature on the second phase precipitation. In comparing the precipitated amounts of the  $\sigma$  and  $\chi$ -phases at interpass temperatures of 50 °C, 150 °C, and 250 °C, this study aims to investigate the effect of second phase precipitation on corrosion characteristics using potentiodynamic polarization and double loop electrochemical potentiokinetic reactivation (DL-EPR) testing.

## 2. TEST METHOD

### 2.1 Welding Materials and Method

Gas tungsten arc welding (GATW) was conducted on a pipe-shaped super duplex stainless steel specimen of 11.9 T thickness, 6-inch diameter, and 200 mm length. The composition of the welding wire was the same as that of the base metal, and Sandvik SAF 2507 steel was selected for use on the basis of ASTM A790 specifications. The chemical composition was measured using an optical emission spectrometer (Metal-Lab75/80J, GNR Srl, Italy), and the resulting values are shown in Table 1. A schematic diagram of the weldment is shown in Figure 1, and a total of nine weld passes were carried out at a bevel angle of 60 °. The welding conditions are detailed in Table 2.

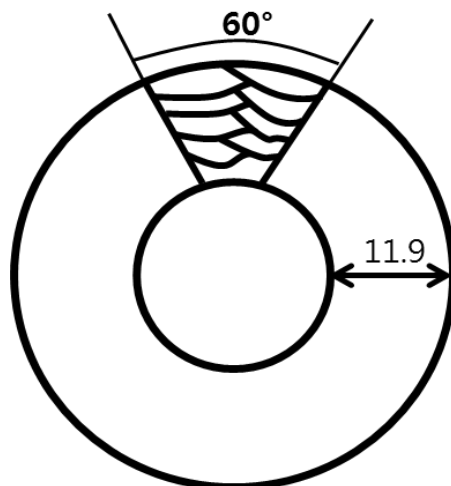


**Figure 1.** Schematic diagram of the weldment. The bevel angle employed was 60 ° and the specimen thickness was 11.9 T.

**Table 1.** Chemical composition of the weld metal (wt%) obtained through optical emission spectroscopy.

	C	N	Si	Mn	P	S	Cr	Ni	Mo
No.1									
No.2	0.018	0.2	0.376	0.343	0.003	0.003	24.5	9.2	3.59
No.3									

**Table 2.** The welding parameters employed in testing.

	Specimen	Voltage (V)	Current (A)	Travel Speed (cm/min)	Heat input (kJ/cm)	Interpass temperature (°C)	Pass
GTAW	No.1					50	
	No.2	9–11	160–175	10	1.0	150	9
	No.3					250	

### 2.2 Microstructure Observation

The microstructure of each weldment was observed using an optical microscope and scanning electron microscope (SEM-EDS, JSM-9400F, Jeol, Japan). After collecting the specimens from the deposited metal, then grinding and polishing these, electrolytic etching was performed. The microstructure was observed at the 2/3 position with respect to the bead surface, and a total of three etching solutions were used. First, in order to observe δ-ferrite and austenite, 10 % oxalic acid was used. The δ-ferrite and austenite were observed to be gray and white, respectively. Next, in order to observe the second phase, electrolytic etching was performed for several seconds at 3 V, using 20 % potassium hydroxide (KOH) aqueous solution. The σ and χ-phases were observed to be yellow and

red-brown, respectively, and the ferrite and austenite were blue-gray and white, respectively. Finally, in order to observe carbides and nitrides, electrolytic etching was performed using a 10 %  $\text{NH}_4\text{OH}$  solution.

Furthermore, using electron backscattering diffraction (EBSD) analysis enabled us to determine the fractions and precipitation trends of  $\delta$ -ferrite and austenite in the deposited metal, as well as those of the second phases, through orientation image mapping (OIM). Test conditions of a 20 kV acceleration voltage and a 6.0 spot size were employed.

### 2.3 Electrochemical Test

Electrochemical testing was performed using a VersaSTAT 3 device (potentiostat/galvanostat, Princeton Applied Research, USA), with specimens that were ground with 2000-grit SiC paper, then cleaned using flowing water; ultrasonically cleansed with ethanol; then dried and used. Corrosion resistances were compared using potentiodynamic polarization testing and DL-EPR testing. The potentiodynamic polarization test was conducted in 0.5 M NaCl at 20 °C, in conditions similar to those of seawater, and the scan rate was maintained at 0.5 mV/s. In order to obtain the  $E_{\text{pitt}}$  value, the average value of three tests was used. In order to measure the degree of sensitization for intergranular corrosion (IGC), testing was conducted in a 2 M  $\text{H}_2\text{SO}_4$  + 1.5 M HCl solution at 20 °C, according to the International Organization for Standardization (ISO) 12372 convention. The IGC resistance was evaluated by measuring the degree of sensitization (DOS) with the ratio of the maximum anode current density ( $I_a$ ) during current increase, and the maximum anode current density during current decrease, using the expression:  $(I_r) ((I_r/I_a)*100)$ . Prior to testing, an open circuit potential (OCP) was applied for 10 min in order to form a stable passive film on the specimen surface. There were three types of electrodes used in testing; a reference electrode composed of a platinum film, the standard electrode was an Ag/AgCl/KCl/Sat (0.197 V) electrode, and the operation electrodes were the respective specimens. The K0235 Flat Cell (Princeton Applied Research, USA) was used in testing, and the measured area was 1 cm<sup>2</sup>.

## 3. RESULTS AND DISCUSSION

### 3.1 Microstructure Observation

Figures 2 and 3 display microstructure images of the weldments in specimens fabricated at interpass temperatures of 50 °C, 150 °C, and 250 °C (denoted No.1, No.2, and No.3). In the microstructure image contained in Figure 2, blue ferrite, white austenite, and yellow and red-brown second phases can be observed. In duplex stainless steel, austenite is generally formed in ferrite, and is mainly classified in terms of three modes: grain boundary austenite, which nucleates in the initial ferrite grain boundary; Widmanstätten austenite, which grows from grain boundary austenite toward a grain; and intragranular austenite. The microstructure changes at the duplex stainless steel weldment were very similar to those of the austenite-ferrite transformation that takes place in low carbon-low

alloy steel. In the cases of grain boundary and Widmanstätten austenite, side-plates nucleate and grow at high temperatures first, and intragranular austenite nucleates and grows at low temperatures, requiring a high driving force. All three types of austenite are observed in the microstructure images shown in Figure 2 (a), (b), and (c). Figure 3 shows microstructure images of specimens that were subject to electrolytic etching with 10 % oxalic acid, containing gray ferrite and white austenite. As may be seen from this figure, as the interpass temperature increased, the amount of austenite in the specimens also increased. This increase was due to the fact that at a certain heat input, the cooling rate of the weldment decreased, with the result that the time spent in conditions favorable for austenite formation increased. This then led to an increase in austenite nucleation/growth in the ferrite.[9] Table 3 shows the amount of austenite calculated as a numerical value with respect to area. In the magnified microstructure image displayed in Figure 2(a), yellow and red-brown second phases can be seen. These are second phases ( $\chi$ ,  $\sigma$ ) with a formation temperature range of 600–1000 °C. The  $\sigma$ -phase was composed of high Cr and Mo contents, as well as precipitates formed through the  $\delta$ -ferrite  $\Leftrightarrow \sigma + \gamma_2$  mechanism for eutectoid reaction. As the  $\sigma$ -phase grew, it caused deterioration in corrosion resistance through the formation of surrounding Cr and Mo deficiency regions. This adversely affected mechanical properties such as the hardening phase. Another second phase, the  $\chi$ -phase, also consisted of large amounts of Cr and Mo, but unlike the  $\sigma$ -phase, it was thermally unstable. Because the  $\chi$ -phase had a lower nucleation barrier than the  $\sigma$ -phase, it precipitated from  $\delta/\gamma$  first. This means that the amount of the  $\chi$ -phase decreased as the  $\sigma$ -phase grew, which increased in size by encroaching on the  $\chi$ -phase. Figure 4 shows SEM images of the  $\sigma$  and  $\chi$ -phases. It can be observed that their fractions also increased with increasing interpass temperature, and like the increase in the austenite fraction, these increased due to an increased time spent in the temperature range at which second phases were formed. It was determined that as second phase precipitation increased,  $\delta$ -ferrite decreased by the same amount. The circled areas in Figure 2 (b) and (c) indicate areas of secondary austenite, which was formed through a eutectoid reaction in  $\delta$ -ferrite. Because of a deficiency of Cr and Mo, which are ferrite stabilization elements,  $\delta$ -ferrite close to the second phase is locally transformed into austenite. This is referred to as secondary-austenite as its composition is different to that of conventional austenite. As in the case of second phases, this has a negative effect on corrosion resistance.[10] Figure 5 shows the fraction changes of the second phase with respect to the interpass temperature, in the form of an EBSD phase map. The obtained values are given in Table 4. The measurement position was constant for all passes because it was at a location where second phase precipitation occurred the most, such as the heat-affected zone (HAZ). A previous pass would be exposed to temperatures in the second phase precipitation temperature range by the heat cycle of follow-up welding in a multi-pass welding process. From Figure 5, it can be observed that the blue second phase was precipitated in the  $\delta/\gamma$  grain boundary, and its amount increased as the interpass temperature rose. Since the interpass temperature rose, the cooling rate slowed down, and as exposure time in the precipitation temperature range increased, the second phase fraction also increased. In contrast, it can be seen that the amount of  $\delta$ -ferrite exhibited a relative decrease.

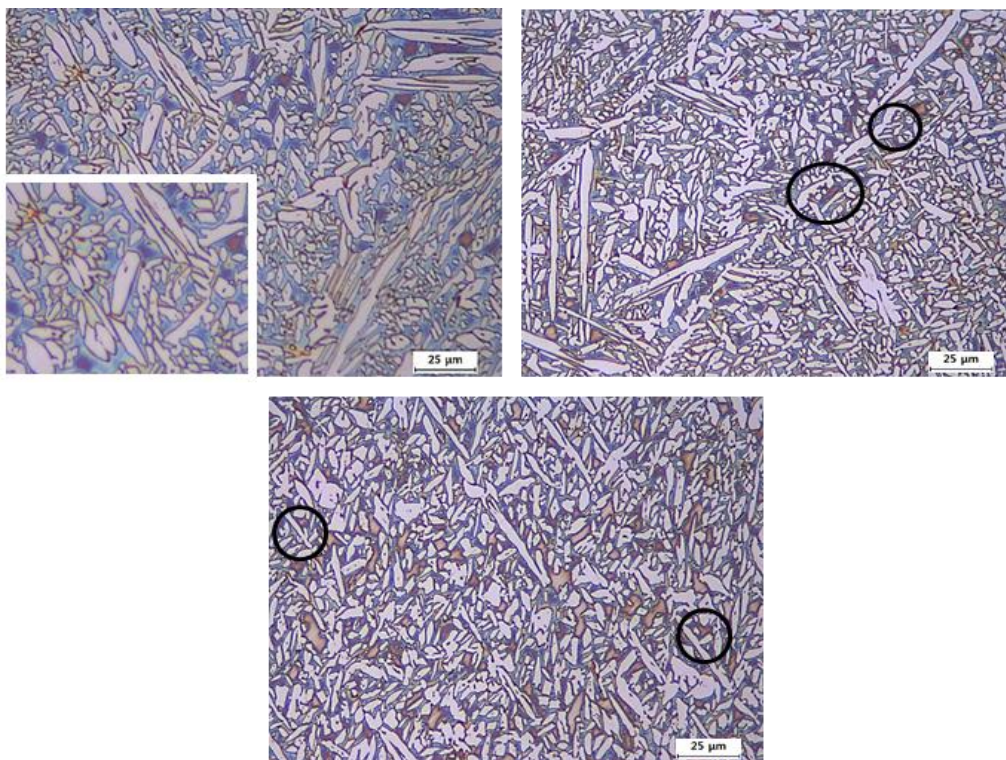


**Figure 2.** Microstructure of the welded metal specimens (a) No.1-50 °C, (b) No.2-150 °C, and (c) No. 3-250 °C, using 20 % KOH solution.

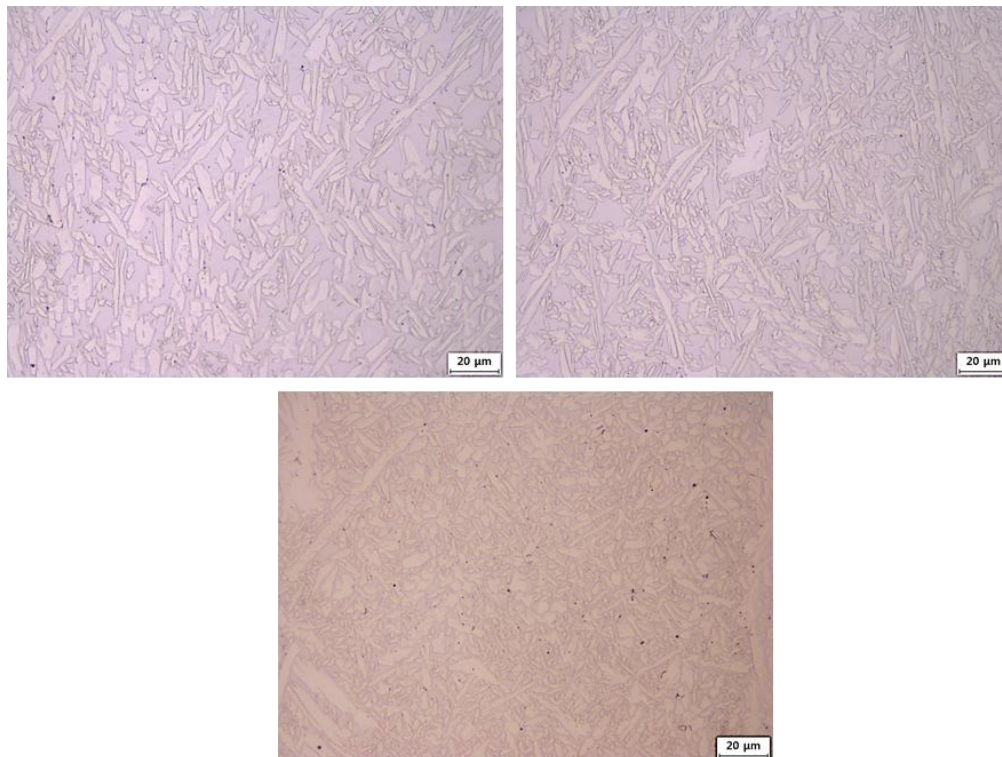


**Figure 3.** Microstructures of the weld metal for specimen (a) No.1-50 °C, (b) No.2-150 °C, and (c) No.3-250 °C, using 10 % oxalic acid.

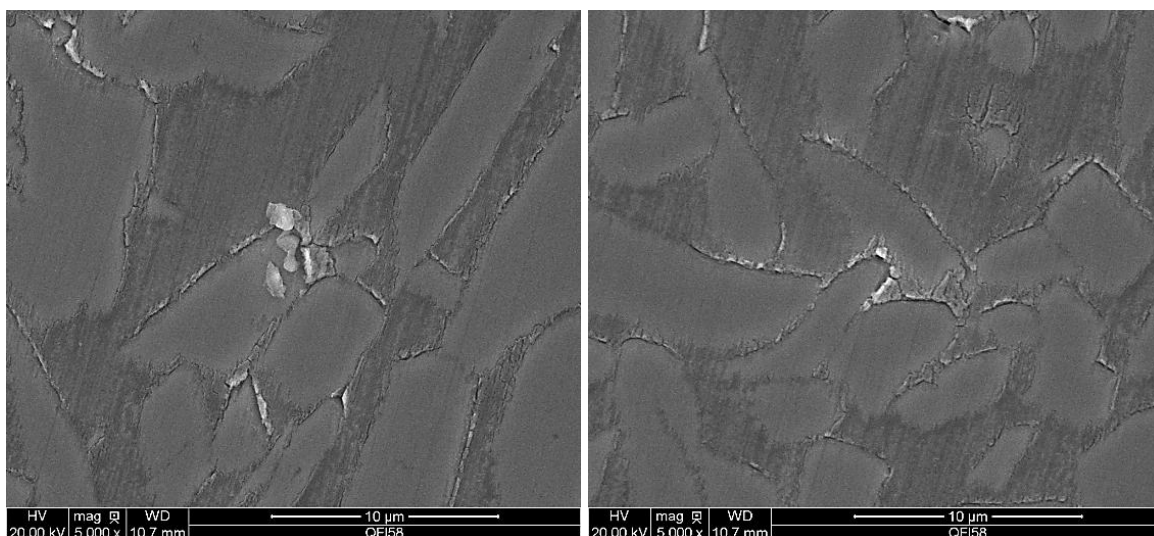


Figure 4. SEM images of the  $\sigma$  and  $\chi$ -phases.

Table 3. The austenite fraction of the specimen weldments.

Specimen	No.1	No.2	No.3
Austenite fraction (%)	45	52	58

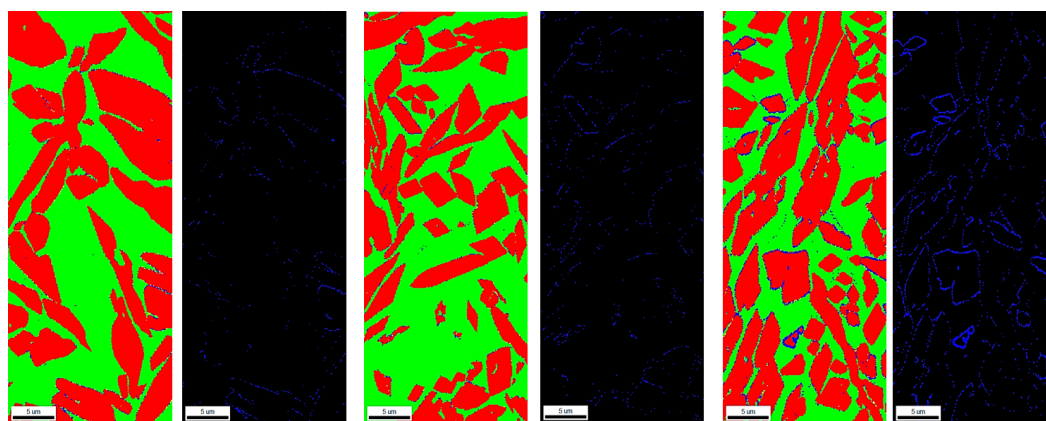


Figure 5. EBSD phase map analysis of specimens (a) No.1-50 °C, (b) No.2-150 °C, and (c) No.3-250 °C.

Table 4. EBSD phase map data for the welded specimens at different interpass temperatures.

Phase	No.1-50 °C	No.2-150 °C	No.3-250 °C
$\gamma$	0.459	0.529	0.575
$\delta$	0.529	0.459	0.387
$\chi$	0.008	0.010	0.036
$\sigma$	0.001	0.008	0.010

### 3.2 Pitting Resistance

In order to analyze the effect of interpass temperature on pitting corrosion resistance, potentiodynamic polarization tests were performed at 25 °C using 0.5 M NaCl solution, and the results are shown in Figure 6. The shape of the polarization curve is similar to those commonly observed for super duplex stainless steel. As the interpass temperature rose, the corrosion potential ( $E_{corr}$ ) and the pitting potential ( $E_{pit}$ ) values shifted toward the negative direction, and the size of the passive zone decreased. A small current peak was observed in the passive zone, which was due to the formation of metastable pitting, since stable pitting was formed and began to spread after the presence of a transpassive current.[11]

The specific corrosion parameters obtained using the potentiodynamic polarization tests are shown in Table 5. The  $E_{pit}$  and  $I_{pit}$  values showed variations according to the interpass temperature; as the interpass temperature increased, these two values decreased. This decrease is related to the amount of precipitation of the second phase. It is generally accepted that the second phase reduces pitting resistance and crevice corrosion resistance, and this is because the Cr and Mo concentrations in the surrounding material are reduced due to the precipitation of second phases, such as the  $\chi$  and  $\sigma$ -phases.[12] Figure 7 shows SEM images of the specimens after the potentiodynamic polarization test. Metastable pit morphologies can be observed mostly in the austenite, with metastable pit sizes of approximately 1–5  $\mu\text{m}$ . This can be explained by the PREN index between the ferrite and austenite, since pitting corrosion resistance improves as the PREN index increases.[13] The PREN value is calculated using the following relation:  $\text{PREN} = \text{wt\% Cr} + 3.3 \text{ wt\% Mo} + 20 \text{ wt\% N}$ , and the PREN index of each phase is shown in Table 6. A comparison of the measured values indicates that the pit was formed in austenite ( $\text{PREN}_{\text{austenite}} = 40.05$ ;  $\text{PREN}_{\text{ferrite}} = 42.78$ ), which had a lower PREN index than ferrite. The SEM micrographs in Figure 7(b) indicate that a pit was formed at the grain boundary in the austenite and ferrite, since the PREN index values of the two phases were similar.[14]

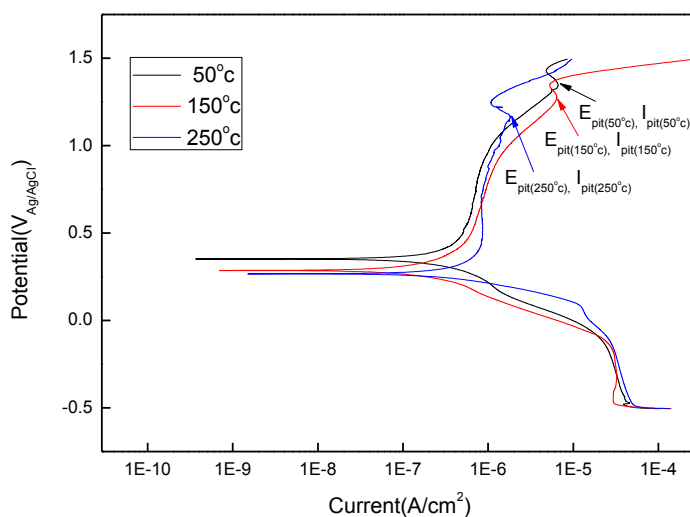


**Figure 6.** The potential versus current density curves obtained using potentiodynamic polarization tests on specimens No.1-50 °C, No.2-50 °C, and No.3-250 °C.

**Table 5.** Corrosion parameters of the SDSS weldments, tested in 0.5 M NaCl solution.

	$E_{corr}$ (mV)	$I_{corr}$ (nA)	$I_{corr}$ (nA/cm <sup>2</sup> )	bc (V/dec)	ba (V/dec)	$E_{pit}$ (V)	$I_{pit}$ ( $\mu$ A)
No.1- 50 °C	351.458	3.558	475.702	0.285	1.714	1.322	6.322
No.2- 150 °C	285.996	6.465	414.522	0.255	1.25	1316	5.731
o.3-250 °C	261.837	10.09	704.074	0.139	1.737	1221	1.186

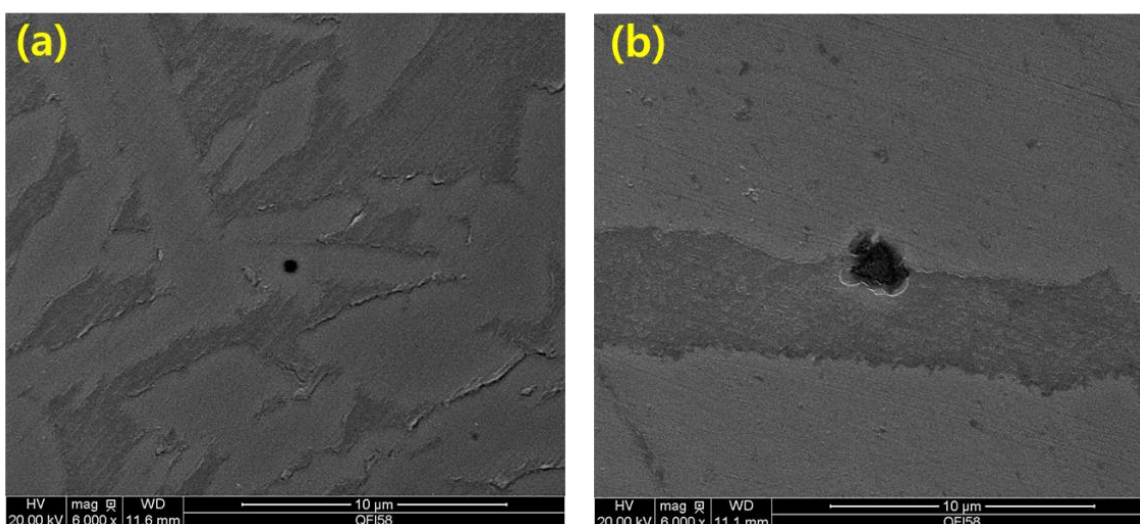


**Figure 7.** Scanning electron micrographs of a pitting attack on specimens after potentiodynamic polarization testing.

**Table 6.** SEM/EDS analysis of each phase in specimen No. 1.

Specimen	Phase	Cr	Ni	Mo	N	PREN
No.1-50 °C	Austenite	24.89	10.43	3.20	0.25	40.45
	Ferrite	26.67	8.17	4.58	0.05	42.78
	Austenite	24.67	10.22	3.5	0.24	41.12
	Ferrite	25.23	8.21	4.7	0.03	41.34

### 3.3 Critical Corrosion Resistance

In order to analyze the effect of interpass temperature on intergranular corrosion, DL-EPR testing was performed at 20 °C in 2 M H<sub>2</sub>SO<sub>4</sub> + 1.5 M HCl solution, and the results are shown in Figure 8. All specimens exhibited similar patterns in their DL-EPR polarization curves. In general, when evaluating intergranular corrosion, the DOS (( $I_a/I_r$ )\*100) is determined by measuring the  $I_a$  and  $I_r$  values during the increase and decrease in the potential, respectively. In general, DOS is thought to have occurred when this value is at least 0.05.[15] Using the calculated  $I_r$  and  $I_a$  values, the DOS was

determined and is given in Figure 9 and Table 7. The DOS values of the specimens increased with increasing interpass temperature. This effect is related to the formation of the second phase, and as the second phase was formed more in the microstructure, a region of lower Cr content occurred around it due to the acceleration of corrosion at the grain boundary. This acceleration in the corrosion was caused by galvanic couple formation between the existing region and the low Cr content region.[16] Figure 10 shows SEM images of the specimens after DL-EPR testing. Although the changes in DOS with respect to the interpass temperature are not visible to the naked eye, it can be observed that intergranular corrosion occurred in areas surrounding the second phase and austenite. The presence of the second phase, with high Cr and Mo content, led to the presence of a surrounding area containing a reduced amount of Cr (Cr deficiency region) during precipitation. In particular, due to the Cr deficiency region around the grain boundary, the Cr oxidized layer was weakened and intergranular corrosion occurred. Figure 11 shows the images of EDS line-scanning of the austenite  $\sigma$ -phase in order to find the Cr deficiency regions, although these regions were not observed. This could be explained by the low resolution of SEM/EDS.[17] The deficiency region of Cr existed around the second phase, but its size was on the order of several nanometers. Meng et al. and Schmuki et al. aimed to analyze the Cr deficiency region using scanning auger microscopy (SAM) with approximately 20 nm resolution, but this attempt was also unsuccessful.[19, 20] In conclusion, the Cr deficiency region could not be found, but when comparing the EBSD phase map and DL-EPR test data, it was found that as the interpass temperature rose, the amount of second phase precipitation increased, and thus, more Cr deficiency regions must have been formed at the grain boundary. Therefore, the oxidized layer of the grain boundary became weaker and intergranular corrosion became more active.

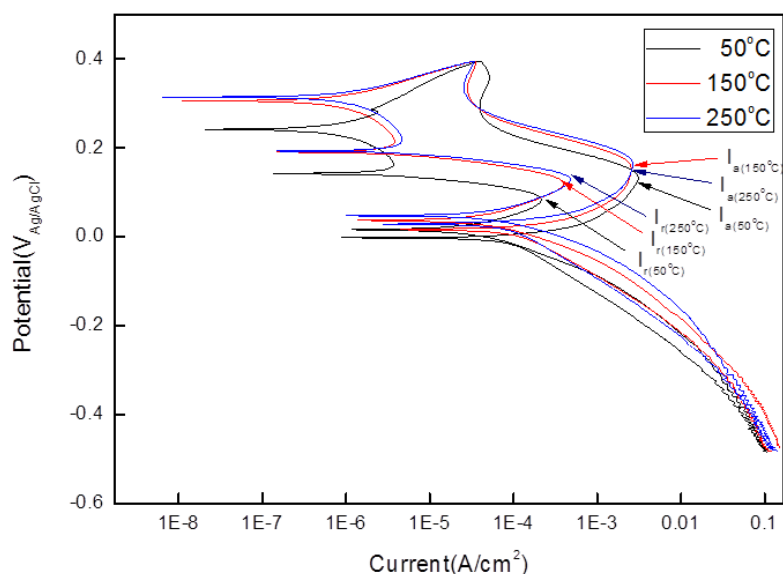


**Figure 8.** The potential versus current density curves obtained using DL-EPR tests on specimens No. 1-50 °C, No. 2-150 °C, and No. 3-250 °C.

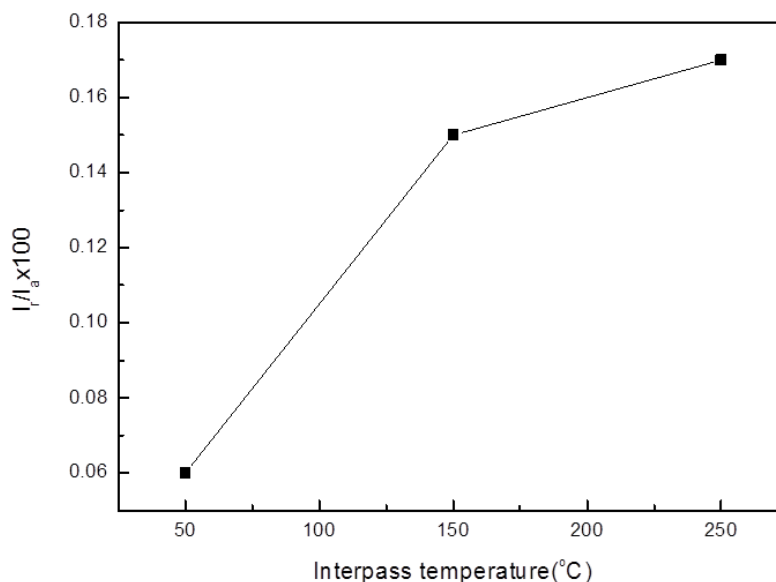


**Figure 9.** Degree of sensitization (DOS) values for different interpass temperatures.

**Table 7.** Degree of sensitization (DOS) data for welded specimens.

	No.1-50 °C	No.2-150 °C	No.3-250 °C
$I_a$	3.0919	2.5381	2.6592
$I_r$	0.2100	0.3905	0.4744
$I_r/I_a \times 100(\%)$	0.06	0.15	0.17

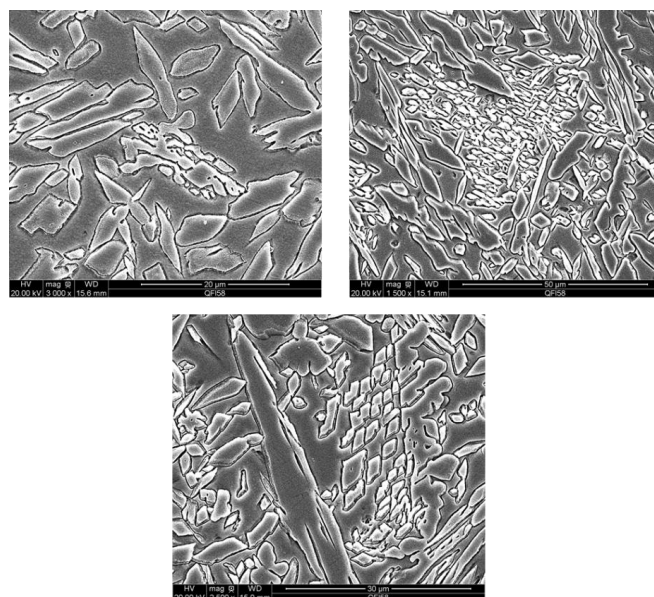


**Figure 10.** Scanning electron micrographs of IGC attack on specimens of different interpass temperatures, after DL-EPR testing. Specimen (top left) No.1-50 °C, (top right) No.2-150 °C, and (bottom) No.3-250 °C.

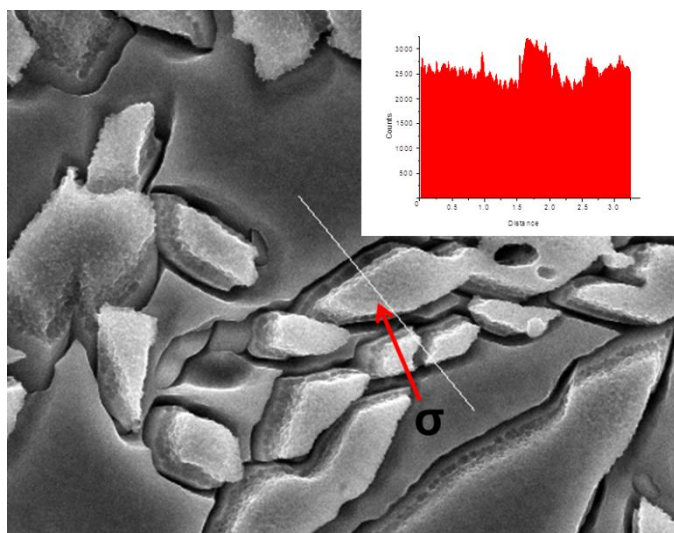


**Figure 11.** Line-scanning image of the  $\sigma$  phase.

#### 4. CONCLUSION

An investigation on the corrosion characteristics of super duplex stainless steels was conducted using interpass temperatures of 50 °C, 150 °C, and 250 °C, and the following conclusions were reached.

1. As a result of phase analysis through the EBSD method, it was determined that as interpass temperature increased, the precipitation of the second phase at the  $\delta/\gamma$  grain boundary increased, and the amount of  $\delta$ -ferrite decreased.

2. The results of potentiodynamic testing indicated that with increasing interpass temperature, the  $E_{\text{pit}}$  value and passive zone size decreased, due to the increase in second phase precipitation in the structure.

3. The formation of pits was related to the PREN index of each phase, and mainly occurred in austenite, which exhibited a low PREN index. However, the formation of pits in ferrite was related to  $\text{Cr}_2\text{N}$  precipitation.

4. The results of DL-EPR testing indicated that as the interpass temperature increased, intergranular corrosion accelerated due to a lack of Cr at the grain boundary, whereas the DOS was subject to increase.

#### ACKNOWLEDGEMENTS

This investigation was supported by the Dong-A University Research Fund

#### Reference

1. H.J. Park, H.W. Lee, *Int. J. Electrochem. Sci.*, 9 (2014) 6687
2. S-K. Ahn, J-S. Kim and K-T. Kim, *Journal of KWS*, 22 (2010) 22
3. V.S Moura, L.D. Lima, J.M. Pardal, A.Y. Kinga, R.R.A. Corte and S.S.M. Tavares, *Materials Characterization*, 59 (2008) 1127

4. S.S.M. Tavares, V.F. Terra, J.M. Pardal and M.P.C. Fonseca, *J Mater Sci.*, 40 (2004) 145
5. T.H. Chen and J.R. Yang, *Mat. Sci. Eng.*, A338 (2002) 166
6. H.Y. Liou, R. Hsieh and W.T. Tsai. *Mater Chem. Phys.*, 74 (2002) 37
7. Y.S. Ahn and J.P. Kang, *Mater. Sci. Technol.* 16 (2000) 382
8. M.E. Wos, V.J Gadgil, J.M. Krougman and B.H. Kolster, *Mater. High Temp.*, 9 (1991) 160
9. M.Q. Johnson, G.M. Evans and G.R. Edwards, *ISIJ International*, 35 (1995) 1222
10. T.H. Chen and H.R. Yang, *Materials Science and Engineering*, A311 (2001) 28
11. M.H. Moayed and R.C. Newman, *Corros. Sci.*, 47 (2005) 1239
12. Y.S Ahn, M. Kim and B.H. Jeong, *Mater. Sci. Technol.*, 16 (2000) 382
13. G. Lothongkum, P. Wongpanya, S. Morito, T. Furuwara, and T. Maki, *Corros. Sci.*, 48 (2006) 137
14. R.A. Perren, T. Suter, C. Solenthaler, G. Gullo, P.J. Uggowitzer, H. Bohni and M.O. Speidel, *Corros. Sci.*, 43 (2001) 727
15. A.J. Sedriks, *Corrosion Of Stainless Steel*, Wiley, Inc. (1996)
16. D.A. Jones, *Principles and Prevention of Corrosion*, Prentice Hall, Inc. (1996)
17. D.W. Kang, H.W. Lee, *Int. J. Electrochem. Sci.*, 9 (2014) 5864
18. M.P. Ryan, D.E. Williams, R.J. Chater, B.M. Hutton and D.S. Mcphail, *Nature*, 415 (2002) 770
19. Q. Meng, G.S. Frankel, H.O. Colijin and S.H. Goss, *Nature*, 424 (2003) 389
20. P.Schmuki, H. Hildebrand, A. Friedrich and S. Virtanen, *Corros. Sci.*, 47 (2005) 1239

© 2015 The Authors. Published by ESG ([www.electrochemsci.org](http://www.electrochemsci.org)). This article is an open access article distributed under the terms and conditions of the Creative Commons Attribution license (<http://creativecommons.org/licenses/by/4.0/>).